Analysis of Multiple Myeloma Drug Efficacy

Alexandre Matov[1, †]

[1] DataSet Analysis LLC, 155 Jackson St, San Francisco, CA 94111

[†] Corresponding author:

email: matov@datasetanalysis.com

Key words: Small RNA, Longitudinal Analysis, Exosomes, Drug Resistance, Disease Detection, Early Disease, Residual Disease, Quantitative Imaging

ABSTRACT

Multiple myeloma (MM) is an incurable plasma cell neoplasm. MM-specific alterations in methylation status cause gradual epigenetic changes and lead to pre-MM disease states, such as Monoclonal Gammopathy of Undetermined Significance (MGUS) and Smoldering MM (SMM). The communication between MM cells and the bone marrow (BM) stromal cells serves a pivotal role in MM development by supporting transformed cell growth and proliferation. MM cells are known to modify the BM microenvironment through secretion of exosomes, which enhances disease progression by the induction of angiogenesis, immune suppression as well as drug resistance. This form of intercellular communication is thought to be mediated by several types of cargo molecules prevalent in exosomes, including microRNAs (miRNAs).

The main obstacle in the treatment of MM is the difficulty in eliminating the residual cancer cells. Even if there are multiple treatment options, none is curative, and remissions have an unpredictable relapse onset. We attempt to address the two hurdles in terms of the difficulty in predicting the duration of remission and the challenge which currently remains out of reach, treatment regiments which guarantee cancer-free bone marrow.

INTRODUCTION

One avenue to address the difficulty in anticipating drug resistance is the *ex vivo* treatment analyses of patient-derived primary cells imaged by multi-color high resolution time-lapse live-cell confocal microscopy to track the motion of exosomes as well as the changes in histone morphology after acetylation. The rates of MM cells exosome secretion are regulated by a variety of genes (Fig. 1) and changes in the rates of secretion can be correlated with drug response and, thus, predict resistance to therapy. Further, the associated with drug treatment changes in the rates of exosome secretion, such as the

number of new particle trajectories as well as the speed of their motin on the cell surface membrane during secretion before and after drug treatment.

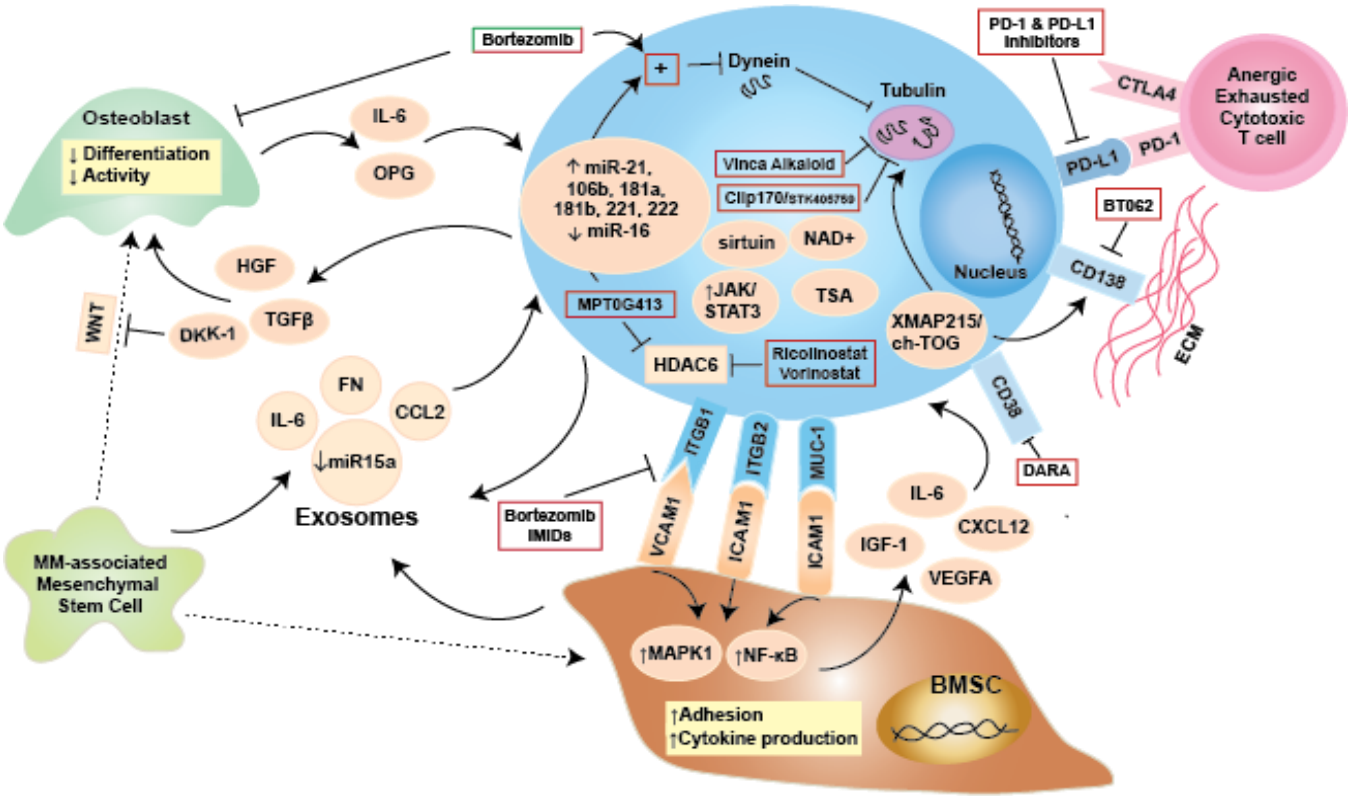

Figure 1. Regulation of drug resistance in multiple myeloma. The myeloma cell is in blue and the interplay with cellular and other components is depicted on the schematics.

URINARY NUCLEIC ACIDS

We performed longitudinal analysis of body fluids with the objective of monitoring gradual changes (Fig. 2) in the regulation of the bone marrow expressed in alteration in the abundance levels of nucleic acids such as miRNAs (Pichiorri et al., 2008; Roccaro et al., 2009). Longitudinal analysis of nucleic acids will allow for the development of novel targeted drugs, such as the liver-specific miRNA-122 inhibitor miravirsen (Gebert et al., 2014). Recent literature has described a plethora of examples of miRNAs that could be targeted in disease. Therefore, monitoring of their levels in healthy individuals (Matov, 2024d) and patients undergoing disease treatment will likely provide valuable datasets for the pharmaceutical industry as well as for practicing physicians, ultimately allowing them to select the most efficacious

treatment sequence and drug combinations for each patient. Our current focus is the identification of personalized biomarker panels whose measurable changes, exceeding the intrinsic stochastic variability in the post-transcriptional regulation of gene expression in normal physiology, uniquely define the degenerative diseases at an early stage when better treatment options are available.

Our aim is to outline a rational for overcoming drug resistance in MM by sensitizing tumor cells with small molecules which correct the dysregulated miRNAs which have been associated with refractory disease. As pre-cancerous changes in methylation status have been linked to changes in the miRNAs abundance levels, one could also investigate the pre-myeloma epigenetic changes to test whether they can be reversed also by targeting the dysregulated miRNAs.

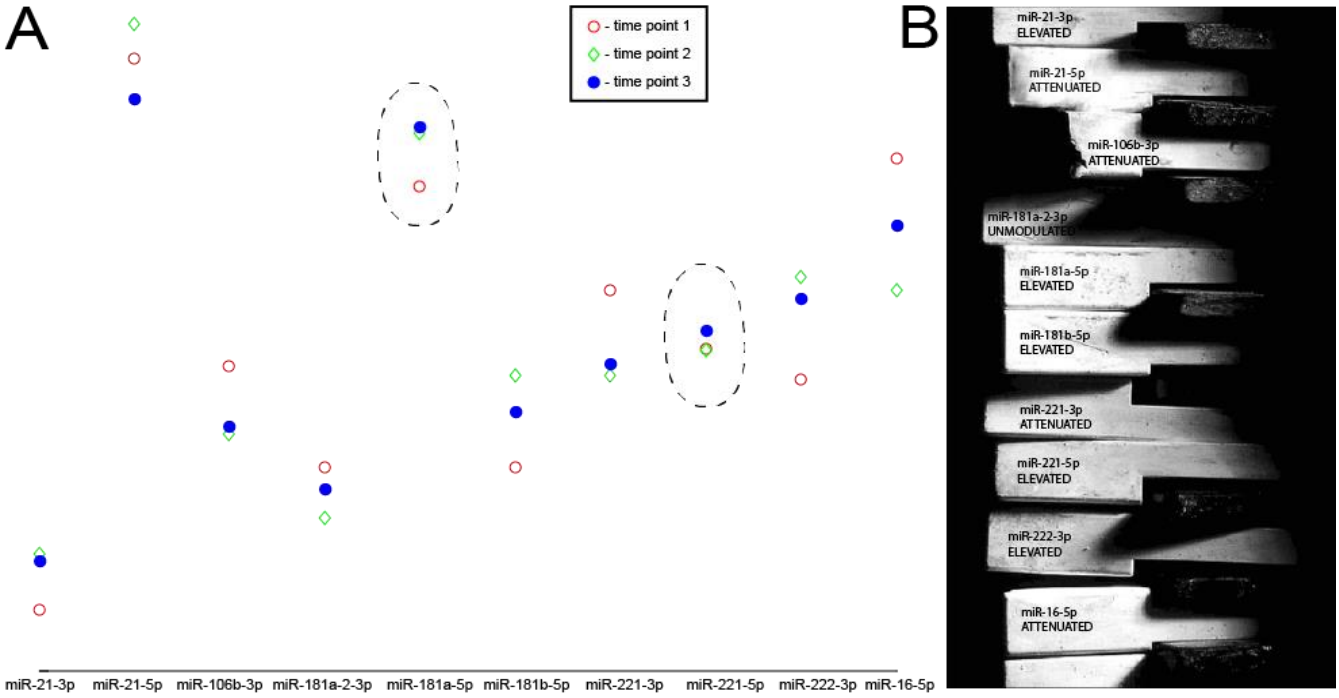

Figure 2. An established panel of miRNAs deregulated in multiple myeloma which are also identified in our preliminary urine data. (A) Based on the list of established biomarkers for multiple myeloma, we show the changes occurring for one person over three time points taken at two months intervals. All biomarkers but the last one are upregulated in multiple myeloma (see also the miRNAs inset on Fig. 1 and (Pichiorri et al., 2008; Roccaro et al., 2009)); therefore, for this particular subject, two biomarkers, miR-181a-5p and miR-221-5p (both encircled on the figure), albeit minimally, are changing toward a disease state (see color-coding figure legend for time progression labeling). (B) Schematic representation of the dysregulation of miRNAs in multiple myeloma; therapeutic strategies can be designed to apply drug treatments which change the miRNAs' abundance levels toward correcting the expression of their underlying gene. Longitudinal analysis of urine samples can, thus, provide a non-invasive drug efficacy readout assay.

MM (Palumbo and Anderson, 2011) remains incurable – a fact underscored by a large number of drugs (available as 37 combinations and counting) used to treat the disease. The available drugs belong to categories chemotherapy (Child et al., 2003), steroids (McIntyre, 1979), immunotherapy (Garfall et al., 2015), proteasome inhibitors (Anderson, 2009), histone deacetylase inhibitors (Hideshima et al., 2016; Prince et al., 2008), and monoclonal antibodies (Raje and Longo, 2015), and drugs from different categories (Laubach, 2019) are used together as combination therapies. Dexamethasone, for instance, is a corticosteroid medication offered for the treatment of relapsed/refractory MM in combinations with different classes of drugs like plitidepsin, selinexor, carfilzomib, daratumumab, lenalidomide, and bortezomib, which have different mechanisms of action (Attal et al., 2017; Chari et al., 2019; Facon et al., 2019; Landgren et al., 2019; Spicka et al., 2019). The complexity of the MM regimens (Choudhry et al., 2018) highlights the incredible ability of the malignant plasma cells to survive and suggests the need to develop quantitative methods for evaluation of both the short- and long-term effects of drug regimens on their cellular target before initiating treatment. Elucidating the specific molecular mechanisms of drug resistance will allow for a better understanding of the reasons behind the failure of all existing treatment regimens to cure MM. In this context, the utilization of a real-time computer vision system (Matov, 2024c) which can reliably evaluate drug action *ex vivo* will also provide an additional platform for functional testing of putative compounds and combination therapies.

ANALYSIS OF EXOSOMES

Optimal drug selection is a challenging task and has been the topic of multiple investigations (Belloni et al., 2018; Candini et al., 2019; Geisler, 2019), and it has become clear that gene expression profile alone is inadequate in predicting therapeutic response (Amin et al., 2014). An image analysis system for drug selection in MM (Silva et al., 2017) has been shown to automatedly enumerate the dead cells using brightfield microscopy at a low spatial and temporal resolution, but *ex vivo* systems for high spatial and temporal resolution analysis are still missing.

Answers about the potential efficacy of a drug can, thus, be obtained by using software systems that measure, in great detail, the effects of a regimen on its cellular targets (Matov, 2024a). Molecular manipulations of living patient-derived cells *ex vivo* can reveal which secondary mechanisms would be activated after a particular drug intervention. To achieve this end, the tracks obtained during computational motion analysis can be used for disease classification and patient stratification purposes. Depending on the methods used, the resulting analysis images may consist of either flow vectors (Matov, 2024c; Matov et al., 2024) or full trajectories (Applegate et al., 2011; Matov et al., 2010) and can be classified into sensitive or resistant using artificial intelligence (AI) methods. Tracking data image stacks, in the thousands, with tracks of the exosomes visualized, can be utilized for disease classification by training a generative transformer (Ren et al., 2024), or another large language model which takes image patterns as input (Horiuchi et al., 2024). Such computational clinical research can aid the discovery of an optimal drug regimen selection by assigning a sensitive or resistant label to every patient cell analyzed.

To track the motion of exosomes (Fig. 3), we will pre-process images making up the microscopy video and select features (Shi and Tomasi, 1994) for motion tracking on-the-fly. Using this data, we will define exosomes' dynamics signatures to distinguish between drug resistance signaling pathways. For each exosome type, based on different exosome markers, we can extract a set of distinctive key features (Rublee et al., 2011), identify descriptor vectors of the features and compute motion metrics to distinguish between drug-resistant and sensitive profiles in cells derived from patients' BM, and elucidate mechanisms of resistance. After classifying all exosome motion trajectories as sensitive or resistant, within the resistant trajectories, we will assign different classes of motion behavior to differentiate between the mechanisms of drug resistance. Our analysis will allow us to identify the relative contributions of different types of exosomes to different resistance mechanisms and pathways. As the differences between exosomes are reflective of the underlying exosome cell type, our novel research tool will offer a mechanistic insight that will contribute to understanding the variety in tumor cell response. This analysis will, therefore, allow for

the identification of the key signaling pathways involved in resistance, which may contribute to the personalization of drug regimens and the functional testing of putative compounds. This computational tool will allow supplementing existing genetic tools with an orthogonal approach to elucidating drug resistance in quantitative detail based on the phenotypical changes in the intracellular communications between tumor cells and their immediate microenvironment. A key novelty is that our computational platform outputs results in real-time during image acquisition (Matov, 2024b), which will facilitate and speed up research efforts by providing instant delivery of data and statistical analysis.

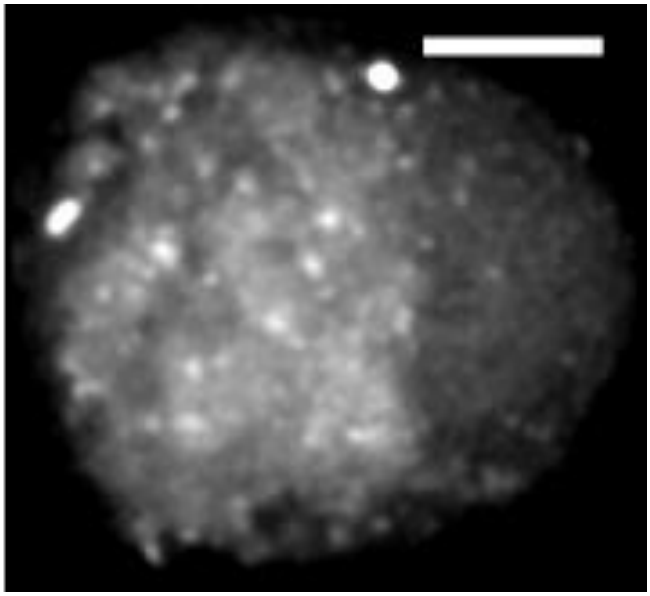

Figure 3. Exosomes in a multiple myeloma cell. Spinning-disk confocal image of the suspension MM1S cell lines acquired five days after labeling with CD63-RFP. A grayscale maximal intensity projection image was aggregated from 20 z-sections to display the 3D volume of exosomes in 2D. The image has been processed with a low pass filter with a cut-off (σ = 1.25) corresponding to the optical limit of the collection frequencies based on the diffraction limit of a 1.45 NA objective. For visualization purposes, the low intensity values were computationally clipped. Scale bar equals 5 µm.

Currently, most patients receive very similar upfront regimens regardless of genotype or phenotype. Very little, if any therapy, is genome-guided, except perhaps for the intensity of upfront therapy as a function of prognostic markers. The genetic analysis process does not involve a microscopic consideration of drug-target engagement at the cellular level. There are multiple factors that pre-determine the ability of a particular drug to engage its target effectively. Important is the ability to precisely measure and provide statistical analysis of the intercellular communication between primary tumor cells under drug treatment in a lab setting. Even if initial treatments induce a state of remission, the disease eventually returns (Lonial, 2010) and, in most cases, does respond to other therapies, even though resistant to the previously given

one. This type of drug response indicates that it is important to develop tools for an upfront optimal drug selection from the presently available treatment options at the onset of therapy.

Our aim is to dissect the changes in the MM cell after treatments at a microscopic level. We will use an approach for *ex vivo* anticipation of drug resistance based on the (i) *ex vivo* evaluation of IC50 values for MM cells treated in a microfluidics device and (ii) changes in live-cell behavior in terms of morphology (Matov and Modiri, 2024) and dynamics (Matov, 2024a) of cellular, molecular markers over 24 hours or longer. In this context, we will rely on a statistical analysis of large populations of molecular markers over an extended period of time to distinguish between disease phenotypes, which otherwise appear similar based on the currently utilized patient stratification methods.

Exosomes are critical to the progression of cancer through the transport of a variety of molecular cargos, including proteins, lipids, and nucleic acids. MM cell‑derived exosomes promote BM stromal cells viability, induce changes in pro‑survival pathways, and the inhibition of their uptake suppresses the functional response in BM stromal cells (Zheng et al., 2019). Cellular exosome uptake depends on cholesterol-rich membrane micro-domains called lipid rafts (Plebanek et al., 2015). Despite recent advances in treatment, MM remains an incurable malignancy, and *in vitro*, *ex vivo* and *in vivo* approaches have identified lipid rafts to constitute a new target in MM (Mollinedo et al., 2010). Novel compounds target and accumulate in MM cell membrane rafts, inducing apoptosis through the co-clustering of rafts and death receptors. Raft disruption by cholesterol depletion inhibited drug uptake by tumor cells as well as cell killing (Plebanek et al., 2015). Modulation of cholesterol flux can, therefore, lead to potent inhibition of tumor cell-derived exosomes, which could deliver a marker for *ex vivo* testing of drug uptake**.** Exosomes produced by MM cells have been shown to promote angiogenesis and immunosuppression, both crucial events in MM progression (Wang et al., 2014). Microfluidics-based platforms (Aleman et al.,

2019; Zhang et al., 2014) are utilized for *ex vivo* culturing of primary MM cells to emulate the dynamic physiology of the bone niche.

We generated preliminary imaging data using 3D spinning disk confocal microscopy with the glucocorticoid-sensitive cell line MM1S (Greenstein et al., 2003) without a drug and after a 24-hour treatment with dexamethasone at concentrations of 60 nM, 120 nM, and 250 nM (the lab IC50 value is 300 nM (Matulis et al., 2016)). To obtain preliminary data, we performed overnight lentiviral transduction and were able to observe the expression of the fluorescent tetraspanin exosome marker CD63-RFP (enriched in extracellular proteins) (Lotvall et al., 2014) 16 hours post infection, which suggests that we could deliver a phenotypical evaluation of the drug-treatment regimen which overcomes the drug resistance mechanisms in refractory disease within a week of patient biopsy collection.

To compute a faithful representation of the image stack within the entire time-lapse sequence, we will utilize SIFT 3D (Scovanner et al., 2007) and Fig. 4 shows our preliminary results for computing SIFT 3D Flow (Liu et al., 2011). To simultaneously optimize both the segmentation and assignment steps, we will utilize a 3D CNN (Hou et al., 2019) using separable convolution with dilation, which is suitable for real-time analysis. Adding dilation rates will allow us to capture multi-scale feature representations without significantly increasing the computation cost of 3D convolution. Because of the low signal-to-noise ratio in the high-resolution exosome images due to photobleaching, we expect false-negative selections during the image segmentation phase. In this context, we will utilize a Bayesian algorithm, which addresses the problem of decision-making given incomplete information. Incomplete information could arise from datasets where certain features are missing in various locations. Importantly, through Bayesian methods, decision-making with uncertainty estimates can be produced (Chandra et al., 2019). Further, as an improvement to spinning disc confocal microscopy, we will perform 3D imaging using lattice light-sheet

microscopy to image intercellular communication via exosomes to ensure a minimal damage to the cells and long-term imaging without photobleaching at comparable x-y-z resolution limits (Chen et al., 2014).

FERROPTOSIS AND ELIMINATION OF RESIDUAL DISEASE

Ferroptosis has a dual role in cancer. It plays a role in tumor initiation, tumorigenesis, which depends on inflammation-associated immunosuppression triggered by ferroptotic damage (Chen et al., 2021) and later, during treatment, in tumor suppression (Hangauer et al., 2017).

We sought to identify therapeutically exploitable vulnerabilities in cancer cells. Initial data obtained with a metastatic (resected from the sternum) rectal cancer organoid with the standard first line metastatic colorectal cancer chemotherapy FOLFOX. We plated organoids with diameters 40-60 µm in 24 wells and performed titration with concentration of 1 µM, 10 µM and 100 µM for two weeks. We repeated

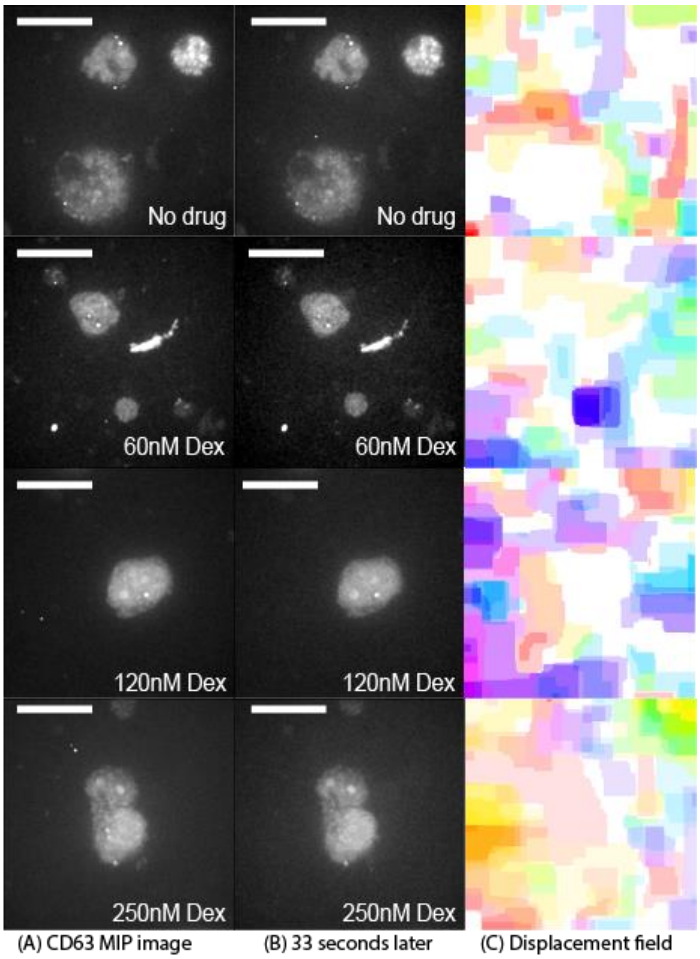

Figure 4. 3D SIFT displacement field analysis of exosome images of untreated cells and of cells 24 hours after treatment with 60 nM, 120 nM or 250 nM dexamethasone. Spinning-disk confocal images of cells from the suspension MM1S cell line at high resolution. Images were acquired 11 days after labeling with CD63-RFP via lentiviral transduction, and for some cells, was performed a 24-hour titration with dexamethasone at concentrations 60 nM, 120 nM, and 250 nM. 3D z-stacks, consisting of 20 2D slices with a 500 ms exposure time at a 2 µm vertical spacing, were acquired. The lateral resolution of the objective is 220 nM. The temporal frequency with which the 3D image stacks were obtained was 11 seconds. Maximal intensity projection (MIP) images were generated in which every pixel has the highest intensity value from the z-axis vector for each x-y position. This transformation allows for the visualization of the combined 3D volume of exosomes in a 2D figure. For evaluation of the 3D SIFT Flow and displacement fields, adjacent in time 2D slices were combined in single 3D files/triplets. Thus, the displacement computation between (A-B) is done over a period of 33 seconds. The cells were immobilized with poly-l-ornithine for imaging. For this reason, a vast proportion of the SIFT flow measured and displayed in (C) is due to the diffusion of culture medium. To visualize the flow fields in (C), each pixel denotes a flow vector for which the angular orientation and magnitude value are represented by the hue and the saturation of the pixel, respectively. Scale bar equals 10 µm.

the same with docetaxel with concentration of 100 nM and 1 µM (Fig. 5), and the experiment showed clear residual disease measured by CellTiter-Glo assay (ATP luminescence had values of up to 6,000 – not shown). This was the first example of "persister" cancer cells in 3D patient-derived organoids cultured in 30 µL Matrigel (Corning) drops, i.e., in their natural 3D environment (Fig. 5) and not as single patient cells cultured on a flat plastic surface in a 2D Petri dish. The state of persistence was initially identified in

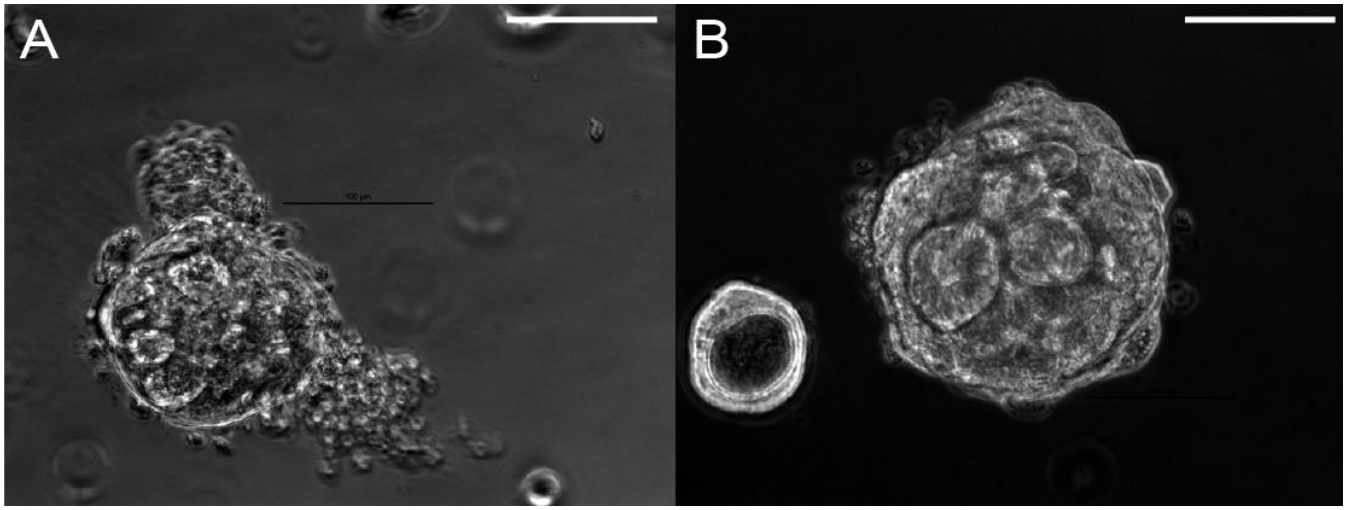

Figure 5. Metastatic rectal cancer organoids receding in dimeter after a 48-hour treatment with docetaxel at 1 µM. (A) The organoid has shrank about twice in size after drug treatment. Crypts are still visible. Many dead cancer cells are visible around the receded organoid. (B) Crypts are clearly visible on this image and even if the organoid edges are still intact, they appear very uneven due to the docetaxel treatment. Scale bars equal 100 µm. Phase contrast microscopy, 20x magnification.

bacterial antibiotic resistance and it is a non-mutational mechanism of acquired drug resistance (Fisher et al., 2017) during which a small population (<5%) of the cells become quiescent. In cancer, the quiescent surviving persister cells minimize the rates of proliferation and, thus, become not susceptible to treatment with mitotic inhibitors and targeting therapies. This reversible process of becoming drug-tolerant is linked to upregulation of mesenchymal markers and downregulation of epithelial markers in the persister cells. During drug holiday, the cells revert to normal metabolism and expand their population, while becoming again susceptible to drug treatment. This cycle repeats multiple times during patient treatment. While the tumor is under drug pressure, however, the few drug-tolerant persister cells pay a metabolic price and become temporarily vulnerable to GPX4 inhibition (Hangauer et al., 2017). Targeting these persister cells

eliminates residual disease and, thus, impedes tumor relapse. Going forward, we envisage to use persister cells derived from tumor organoids as a discovery platform to identify therapeutic agents that can eliminate residual persisters that remain after initial successful cytotoxic drug treatment.

During the first few days of drug treatment, the rectal organoids retained their distinct morphology (Fig. 5). One possible approach to evaluate the variety of changes in morphology patterns of whole (treatment-resistant) organoids, after drug treatment, which can also be applied to the analysis of changes in MM histone morphology after acetylation, can be accomplished by texture analysis of organoid images. Such quantitative readout can be used as a biomarker for clinical response therapy in grayscale value images of patient-derived tumor organoids (Fig. 5).

Patient organoids are considered sensitive to treatment when multiple image features changes are statistically significant, such as the shift in metrics related to the organoid edge and the contraction or oblongation of the organoid shape. Using this method, we are correlating changes in organoid images with clinical response to therapy, in order to develop a model predictive of drug response. To develop this computational platform, we started by analyzing microtubule cytoskeleton changes in a panel of docetaxel-sensitive (MKN-45, SNU-1, TMK-1, AZ-521) and resistant (MKN-7, SCH, Hs746T) cell lines. In this context, we examined 20 types of changes, termed features, between cells at base line and after docetaxel treatment (not shown).

A key to the success of an automated system for organoid pattern analysis is the design of suitable numerical descriptors (features) which capture essential information from images without being overly sensitive to variations induced by organoid shape or orientation. Many types of features have been investigated in the field of computer vision and we selected specific features to describe and quantify the changes in organoids during drug treatment, such as Haralick features (angular second moment, pixel

variance, pixel entropy, etc.) (Haralick, 1983) and computation of Zernike moments (shape similarity of organoid images to Zernike polynomials - 49 polynomials and 49 features) (Boland and Murphy, 2001). Additional features which can be computed pertain to organoid morphological features, organoid edge features, the morphological skeleton, and convex hull. The morphological features comprise of the number of bright objects in the organoid image, Euler number of the organoid image, average bright object size, variance of object size, to name a few. The edge related features are the fraction of above an intensity threshold pixels along the organoid edge, the homogeneity of the gradient of organoid edge intensity, homogeneity in the direction of the organoid edge, and other. The morphological skeleton features are the average length of the morphological skeleton of the organoids, the ratio of the number of branch points in the morphological skeleton to the overall length of the skeleton, and other. The convex hulls features consist of organoid eccentricity, the roundness of the organoid convex hull, and the fraction of the organoid convex hull pixels above an intensity threshold.

Our results after docetaxel treatment show that in populations of sensitive cells a high number of (25%-60% of all) features undergo statistically significant shifts. This shows that an affected microtubule network correlates with drug-target engagement and response. Moreover, sensitive cells exhibit changes in different subsets of features suggesting different underlying mechanisms of docetaxel sensitivity. Oppositely, after treatment of resistant cells with docetaxel, a change in a very few (0%-5%) of the features was a hallmark of resistance.

We also derived drug-tolerant persister cells in prostate cancer (MSK-PCa3) 3D organoids (Gao et al., 2014), which were obtained at MSKCC from tumor resection at a retroperitoneal lymph node after receiving prior therapy with ADT, bicalutamide, docetaxel, and carboplatin, i.e., the tumor was refractory to both hormonal and systematic therapy. We tested therapeutic treatments to kill these persisters. Due to a disabled antioxidant program, persister cells are unable to tolerate lipid hydroperoxide accumulation and

are susceptible to ferroptotic drugs (Hangauer et al., 2017). To achieve this end, we performed experiments showing that cells derived from two to seven weeks of docetaxel treatment are sensitive to the novel compounds RSL3 and ML210, both small molecule GPX4 inhibitors.

We, therefore, sought to test if the small molecule ML210 is electively toxic to persister cells without inducing significant toxicity in parental organoid MSK-PCa3 cells. Organoids with diameter 40-60 µm were plated in 12 wells and half of the wells were treated for five weeks with ML210 at 5 µM. After five weeks of organoid culture and reaching a phase of exponential growth, the organoids had diameter size of 60-600 µm (Fig. 6). The differences in numbers of viable cells between the untreated organoids and the ML210-treated wells were not statistically significant, which demonstrated that ML210 was not toxic to the parental cancer organoid cells.

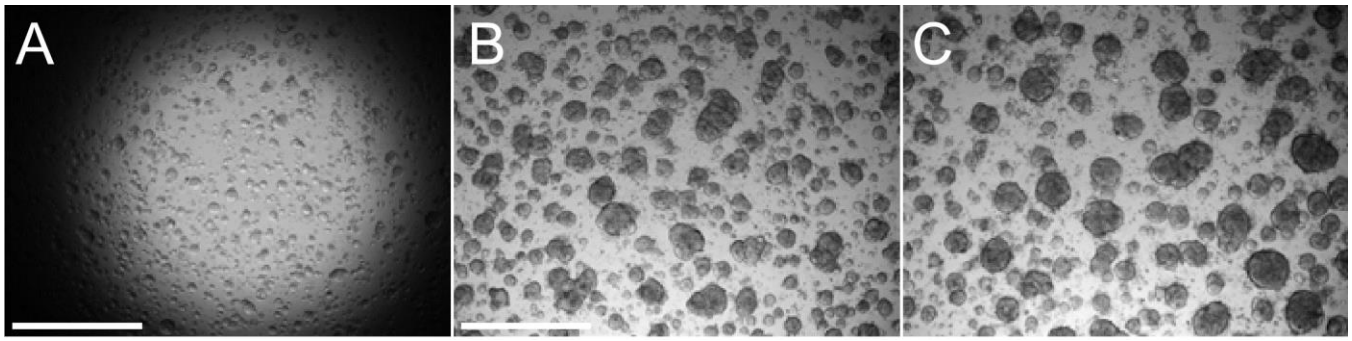

Figure 6. Lymph-metastasis patient-derived prostate cancer organoids after no treatment and after treatment with a ferroptosis inhibitor only. Organoids with diameter 40-60 µm were plated in 12 wells and half of the wells were treated for five weeks with ML210 at 5 µM. After five weeks of culturing, the organoids had diameter size of 60-600 µm. Overall, the differences in numbers of viable cells between the control cells and the ML210 treated cells were not statistically significant, which demonstrates that ML210 requires docetaxel-induced persister state to be toxic to the parental cancer organoid cells. (A) Image of organoids at baseline. (B) Image showing the organoids after five weeks with no drug added. (C) Image showing organoids after five weeks treated with ML210 only. Scale bars equal 2 mm. Transmitted light microscopy, 4x magnification.

We then plated organoids with diameter 40-60 µm in 12 wells of which four were treated with docetaxel at 100 nM for seven weeks, four wells were treated for two weeks with docetaxel at 100 nM followed by a five-week co-treatment with docetaxel at 100 nM and ML210 at 5 µM, and four wells were treated for two weeks with docetaxel at 100 nM followed by a five-week co-treatment with docetaxel at 100 nM,

ML210 at 5 µM, and ferrostatin-1 at 2 µM (Fig. 7). The organoids had a diameter of 40-60 µm at baseline and the two weeks treatment with docetaxel eliminated the vast majority of the organoid cells and induced a persister state in the residual cancer cells. A follow-up co-treatment with the GPX4 inhibitor ML210 reduced the number of viable residual cells two-fold in median values (a median value of ATP luminescence of 3,000 after seven weeks of docetaxel treatment was reduced to a 1,500 median value – not shown). We measured a significant decrease of 63% in mean ATP luminescence values with only about a third of the persister cells remaining viable after ML210 co-treatment when we compared the numbers of viable cells after seven weeks of docetaxel-only treatment. Further, co-treatment with the lipophilic antioxidants ferrostatin-1 rescued the persister cells from the toxic effects of GPX4 inhibition and we measured a 44% increase in mean cell viability in the wells for which we also added ferrostatin-1 at 2 µM in comparison to the viability of the cells co-treated with ML210 only; however, the median ATP luminescence values for this experiment remained the same, which demonstrates a partial rescue and suggests that higher levels of ferrostatin-1 could rescue more efficiently the persister cells from the toxic effects of GPX4 inhibition. We also observed extensive Matrigel damage in some of the wells with

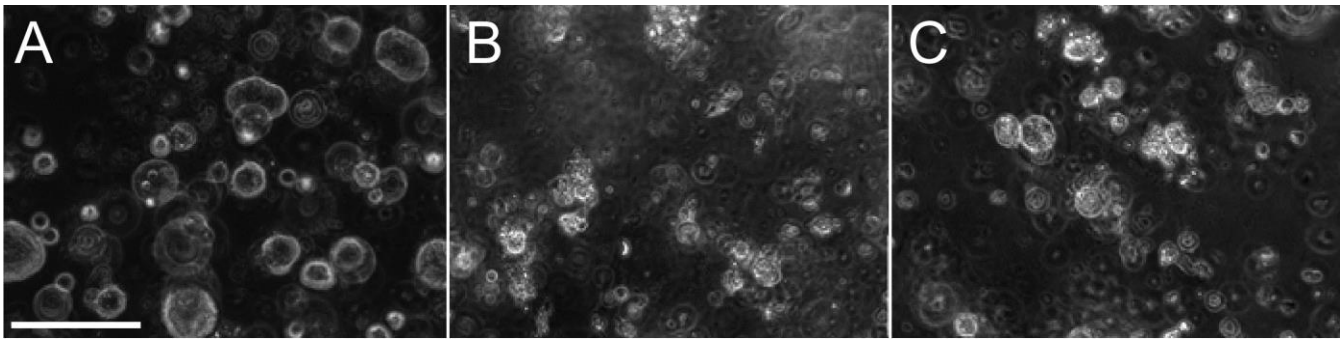

Figure 7. Lymph-metastasis patient-derived prostate cancer organoids before and after treatment with a cytotoxic drug in combination with a ferrortosis-inducing small molecule with or without added rescue drug. (A) Image of organoids at baseline. (B) Image showing dead organoid cells in Matrigel after combination treatment with docetaxel at 100 nM and ML210 at 5 µM. (C) Image taken after treatment with docetaxel at 100 nM and ML210 at 5 µM together with the rescue drug ferrostatin-1 at 2 µM shows very small organoids. Scale bar equals 100 µm. Phase contrast microscopy, 20x magnification.

ferrostatin-1, which likely contributed to the very low cell viability numbers in these particular affected wells; the Matrigel damage likely contributed also to the overall high variability and low statistical significance of the rescue experiment.

Inducing ferroptosis is a viable strategy for the elimination of residual disease in MM as well (Logie et al., 2021). The development of a real-time computer vision system (Matov, 2024b), which can reliably evaluate drug action *ex vivo* will provide an additional platform for functional testing of putative compounds and combination therapies, including those exploiting vulnerabilities in cancer cells, like the susceptibility to ferroptosis—inducing small molecules, to eliminate residual disease. Quantitative imaging could be displayed during tumor board meetings, which would allow the discussion of tentative regimens based on the supporting information provided by the microscopic evaluation of patient-derived cultures.

CONCLUSIONS

The model system we propose can be based on cells extracted from BM biopsies. It can utilize different marrow cellular components to recreate the tumor microenvironment in the lab. Through flow cytometry, several cell types can be selected, based on surface antigens such as CD138 for myeloma, CD34 for stem cells, and CD105 for mesenchymal cells. A BM biopsy could yield about ten million cells and after FACS sorting, one expects to collect about 200k MM cells, 20k stem cells, <100k mesenchymal cells. Patient samples can be obtained by overnight shipping of fresh biopsies at room temperature. At the biopsy site, one would immediately isolate the BM mononuclear cells and then sort for the three markers. The BM cells are suspension cells with diameters of about seven to 15 µm (Orkin and Zon, 2008), and their exosomes have sizes between 20 and 100 nm (Thery et al., 2018). MM/BM cells are extremely sensitive to *ex vivo* culture and die (100% rate) when plated in a standard 2D culture dish. To culture them in the lab, there are culture methods that recreate their 3D microenvironment. To provide a similar environment,

we will culture them on hFOB 1.19 cells, which mimic the human bone, in a specialized microfluidics device. The BM culture medium consists of RPMI with L-glutamine, patient plasma, CaCl2, sodium succinate, hydrocortisone, heparin (Zhang et al., 2015), and one should allow for 48 hours of metabolic recovery after the biopsy before an *ex vivo* drug treatment. After plating patient cells in microfluidics, about 70% of them will survive (Zhang et al., 2014). To increase the rates of patient-cell survival after plating further, we will test additional media components based on novel media formulations to improve the cell viability (Aleman et al., 2019). Lentiviral-mediated expression of the fluorescent exosome markers (Lotvall et al., 2014) CD63-RFP, CD9-GFP, and CD81-YFP can be used to mark exosomes for visualization. A combination of the three tetraspanins can be used to analyze exosomes of different origins, enriched in different, transmembrane or lipid-bound, extracellular proteins.

As the drug response motion trajectory differences between exosomes will be reflective of the cell type, the approach described in this article will offer a mechanistic insight that will contribute to understanding the variety in tumor cell response. Based on clinical data for resistance, this analysis will allow for the identification of an *ex vivo* resistance baseline phenotype and for the characterization of the changes in this phenotype, or lack thereof, after treatments with different drug combinations of refractory samples for which currently there is no known suitable treatment regimen. Furthermore, our method will allow performing quantitative live-cell companion diagnostics by evaluating the relative contribution of different signaling pathways in drug resistance and response via quantitative exosome imaging, beyond MM, in primary tumor cells originating from different organs and tissues, such as acute myeloid leukemia, primary pancreatic, and bone metastatic prostate tumors.

MATERIALS AND METHODS

Sample Processing

Small RNA were extracted from de-identified urine samples by Norgen Biotek Corp.

Cell Culture

Organoids with diameter 40-60 µm were plated in 30 µL Matrigel drops in six wells per condition of a 24-well plate per condition and treated for two or more weeks with docetaxel with concentration of 100 nM and 1 µM to eliminate the vast majority of the organoid cells and induce a persister state in the residual cancer cells. This treatment was followed by co-treatment with docetaxel 100 nM and small molecule ML210 5 µM or docetaxel 100 nM combined with small molecule ML210 5 µM and lipophilic antioxidants ferrostatin-1 2 µM, rescue treatment. ML210, ferrostatin-1 and docetaxel were purchased from Sigma-Aldrich.

Exosomes in MM1S cells (a gift from Michael Plebanek) were visualized by lentivirus-mediated low level expression of CD63-RFP. To generate imaging data, we performed lentiviral infection with CD63-RFP and observed labeling signal in the red channel 16 hours later. We did not use blasticidin selection as the infection rate was over 90% and performed a 24-hour titration with dexamethasone at concentrations 60 nM, 120 nM, and 250 nM.

Microscopy Imaging

We imaged CD63-RFP-expressing MM1S cells by time-lapse spinning disk confocal microscopy using a 100x oil immersion objective and acquired 3D z-stacks, which consisted of 20 2D slices acquired with a 500 ms exposure time at a 2 µm vertical spacing. The lateral resolution of a 1.45 NA objective is 220 nM. The temporal frequency with which we acquired 3D image stacks was 11 seconds.

Organoids were imaged using transmitted light microscopy at 4x magnification and phase contrast microscopy at 20x magnification on a Nikon Eclipse Ti system with camera Photometrics CoolSnap HQ2.

Data Analysis

All data analysis programs and graphical representation of the results were developed in Matlab and R, and available upon request. The 3D SIFT Flow method for 3D displacement fields analysis computation is described and validated in (Liu et al., 2011).

Ethics Declaration

IRB (IRCM-2019-201, IRB DS-NA-001) of the Institute of Regenerative and Cellular Medicine.

Ethical approval was given.

Approval of tissue requests #14-04 and #16-5 to the UCSF Cancer Center Tissue Core and the Genitourinary Oncology Program was given.

ACKNOWLEDGEMENTS

I thank Michael Plebanek for MM1S cells and CD63-RFP virus particles, Arun Wiita and his lab for their help, Anna Celli for 3D imaging help, and JR&D Services for funding in the context of NGS data. I am grateful to the Genitourinary Tissue Utilization committee and the Genitourinary and Prostate SPORE Tissue Cores at the UCSF Cancer Center for the approval of my tissue requests #14-04 and #16-5, the Institute of Regenerative and Cellular Medicine for issuing the Institutional Review Board protocol approval IRCM-2019-201, IRB DS-NA-001 for the observational study “Longitudinal analysis of next-generation sequencing of nucleic acids for early detection of degenerative diseases such as cardiovascular, neoplastic and diseases related to the nervous system” and James Faber for his feedback regarding the protocol and the process of approval.

REFERENCES

Aleman, J., S.K. George, S. Herberg, M. Devarasetty, C.D. Porada, A. Skardal, and G. Almeida-Porada. 2019. Deconstructed Microfluidic Bone Marrow On-A-Chip to Study Normal and Malignant Hemopoietic Cell-Niche Interactions. *Small*:e1902971.

Amin, S.B., W.K. Yip, S. Minvielle, A. Broyl, Y. Li, B. Hanlon, D. Swanson, P.K. Shah, P. Moreau, B. van der Holt, M. van Duin, F. Magrangeas, P. Pieter Sonneveld, K.C. Anderson, C. Li, H. Avet-Loiseau, and N.C. Munshi. 2014. Gene expression profile alone is inadequate in predicting complete response in multiple myeloma. *Leukemia*. 28:2229-2234.

Anderson, K.C. 2009. Proteasome inhibitors in multiple myeloma. *Semin Oncol*. 36:S20-26.

Applegate, K.T., S. Besson, A. Matov, M.H. Bagonis, K. Jaqaman, and G. Danuser. 2011. plusTipTracker: Quantitative image analysis software for the measurement of microtubule dynamics. *J Struct Biol*. 176:168-184.

Attal, M., V. Lauwers-Cances, C. Hulin, X. Leleu, D. Caillot, M. Escoffre, B. Arnulf, M. Macro, K. Belhadj, L. Garderet, M. Roussel, C. Payen, C. Mathiot, J.P. Fermand, N. Meuleman, S. Rollet, M.E. Maglio, A.A. Zeytoonjian, E.A. Weller, N. Munshi, K.C. Anderson, P.G. Richardson, T. Facon, H. Avet-Loiseau, J.L. Harousseau, and P. Moreau. 2017. Lenalidomide, Bortezomib, and Dexamethasone with Transplantation for Myeloma. *The New England journal of medicine*. 376:1311-1320.

Belloni, D., S. Heltai, M. Ponzoni, A. Villa, B. Vergani, L. Pecciarini, M. Marcatti, S. Girlanda, G. Tonon, F. Ciceri, F. Caligaris-Cappio, M. Ferrarini, and E. Ferrero. 2018. Modeling multiple myeloma-bone marrow interactions and response to drugs in a 3D surrogate microenvironment. *Haematologica*. 103:707-716.

Boland, M.V., and R.F. Murphy. 2001. A neural network classifier capable of recognizing the patterns of all major subcellular structures in fluorescence microscope images of HeLa cells *Bioinformatics*. 17:1213-1223.

Candini, O., G. Grisendi, E.M. Foppiani, M. Brogli, B. Aramini, V. Masciale, C. Spano, T. Petrachi, E. Veronesi, P. Conte, G. Mari, and M. Dominici. 2019. A Novel 3D In Vitro Platform for Pre-Clinical Investigations in Drug Testing, Gene Therapy, and Immuno-oncology. *Sci Rep*. 9:7154.

Chandra, R., K. Jain, R.V. Deo, and S. Cripps. 2019. Langevin-gradient parallel tempering for Bayesian neural learning. *Neurocomputing*. 359:315-326.

Chari, A., D.T. Vogl, M. Gavriatopoulou, A.K. Nooka, A.J. Yee, C.A. Huff, P. Moreau, D. Dingli, C. Cole, S. Lonial, M. Dimopoulos, A.K. Stewart, J. Richter, R. Vij, S. Tuchman, M.S. Raab, K.C. Weisel, M. Delforge, R.F. Cornell, D. Kaminetzky, J.E. Hoffman, L.J. Costa, T.L. Parker, M. Levy, M. Schreder, N. Meuleman, L. Frenzel, M. Mohty, S. Choquet, G. Schiller, R.L. Comenzo, M. Engelhardt, T. Illmer, P. Vlummens, C. Doyen, T. Facon, L. Karlin, A. Perrot, K. Podar, M.G. Kauffman, S. Shacham, L. Li, S. Tang, C. Picklesimer, J.R. Saint-Martin, M. Crochiere, H. Chang, S. Parekh, Y. Landesman, J. Shah, P.G. Richardson, and S. Jagannath. 2019. Oral Selinexor-Dexamethasone for Triple-Class Refractory Multiple Myeloma. *The New England journal of medicine*. 381:727-738.

Chen, B.C., W.R. Legant, K. Wang, L. Shao, D.E. Milkie, M.W. Davidson, C. Janetopoulos, X.S. Wu, J.A. Hammer, 3rd, Z. Liu, B.P. English, Y. Mimori-Kiyosue, D.P. Romero, A.T. Ritter, J. Lippincott-Schwartz, L. Fritz-Laylin, R.D. Mullins, D.M. Mitchell, J.N. Bembenek, A.C. Reymann, R. Bohme, S.W. Grill, J.T. Wang, G. Seydoux, U.S. Tulu, D.P. Kiehart, and E. Betzig. 2014. Lattice light-sheet microscopy: imaging molecules to embryos at high spatiotemporal resolution. *Science*. 346:1257998.

Chen, X., R. Kang, G. Kroemer, and D. Tang. 2021. Broadening horizons: the role of ferroptosis in cancer. *Nat Rev Clin Oncol*. 18:280-296.

Child, J.A., G.J. Morgan, F.E. Davies, R.G. Owen, S.E. Bell, K. Hawkins, J. Brown, M.T. Drayson, and P.J. Selby. 2003. High-dose chemotherapy with hematopoietic stem-cell rescue for multiple myeloma. *The New England journal of medicine*. 348:1875-1883.

Choudhry, P., D. Galligan, and A.P. Wiita. 2018. Seeking Convergence and Cure with New Myeloma Therapies. *Trends Cancer*. 4:567-582.

Facon, T., S. Kumar, T. Plesner, R.Z. Orlowski, P. Moreau, N. Bahlis, S. Basu, H. Nahi, C. Hulin, H. Quach, H. Goldschmidt, M. O'Dwyer, A. Perrot, C.P. Venner, K. Weisel, J.R. Mace, N. Raje, M. Attal, M. Tiab, M. Macro, L. Frenzel, X. Leleu, T. Ahmadi, C. Chiu, J. Wang, R. Van Rampelbergh, C.M. Uhlar, R. Kobos, M. Qi, and S.Z. Usmani. 2019. Daratumumab plus Lenalidomide and Dexamethasone for Untreated Myeloma. *The New England journal of medicine*. 380:2104-2115.

Fisher, R.A., B. Gollan, and S. Helaine. 2017. Persistent bacterial infections and persister cells. *Nature reviews. Microbiology*. 15:453-464.

Gao, D., I. Vela, A. Sboner, P.J. Iaquinta, W.R. Karthaus, A. Gopalan, C. Dowling, J.N. Wanjala, E.A. Undvall, V.K. Arora, J. Wongvipat, M. Kossai, S. Ramazanoglu, L.P. Barboza, W. Di, Z. Cao, Q.F. Zhang, I. Sirota, L. Ran, T.Y. MacDonald, H. Beltran, J.M. Mosquera, K.A. Touijer, P.T. Scardino, V.P. Laudone, K.R. Curtis, D.E. Rathkopf, M.J. Morris, D.C. Danila, S.F. Slovin, S.B. Solomon, J.A. Eastham, P. Chi, B. Carver, M.A. Rubin, H.I. Scher, H. Clevers, C.L. Sawyers, and Y. Chen. 2014. Organoid cultures derived from patients with advanced prostate cancer. *Cell*. 159:176-187.

Garfall, A.L., M.V. Maus, W.T. Hwang, S.F. Lacey, Y.D. Mahnke, J.J. Melenhorst, Z. Zheng, D.T. Vogl, A.D. Cohen, B.M. Weiss, K. Dengel, N.D. Kerr, A. Bagg, B.L. Levine, C.H. June, and E.A. Stadtmauer. 2015. Chimeric Antigen Receptor T Cells against CD19 for Multiple Myeloma. *The New England journal of medicine*. 373:1040-1047.

Gebert, L.F., M.A. Rebhan, S.E. Crivelli, R. Denzler, M. Stoffel, and J. Hall. 2014. Miravirsen (SPC3649) can inhibit the biogenesis of miR-122. *Nucleic acids research*. 42:609-621.

Geisler, J.G. 2019. 2,4 Dinitrophenol as Medicine. *Cells*. 8.

Greenstein, S., N.L. Krett, Y. Kurosawa, C. Ma, D. Chauhan, T. Hideshima, K.C. Anderson, and S.T. Rosen. 2003. Characterization of the MM.1 human multiple myeloma (MM) cell lines: a model system to elucidate the characteristics, behavior, and signaling of steroid-sensitive and -resistant MM cells. *Exp Hematol*. 31:271-282.

Hangauer, M.J., V.S. Viswanathan, M.J. Ryan, D. Bole, J.K. Eaton, A. Matov, J. Galeas, H.D. Dhruv, M.E. Berens, S.L. Schreiber, F. McCormick, and M.T. McManus. 2017. Drug-tolerant persister cancer cells are vulnerable to GPX4 inhibition. *Nature*. 551:247-250.

Haralick, R.M. 1983. Ridges and Valleys on Digital Images. *Computer Vision Graphics and Image Processing*. 22:28-38.

Hideshima, T., J. Qi, R.M. Paranal, W. Tang, E. Greenberg, N. West, M.E. Colling, G. Estiu, R. Mazitschek, J.A. Perry, H. Ohguchi, F. Cottini, N. Mimura, G. Gorgun, Y.T. Tai, P.G. Richardson, R.D. Carrasco, O. Wiest, S.L. Schreiber, K.C. Anderson, and J.E. Bradner. 2016. Discovery of selective small-molecule HDAC6 inhibitor for overcoming proteasome inhibitor resistance in multiple myeloma. *Proc Natl Acad Sci U S A*. 113:13162-13167.

Horiuchi, D., H. Tatekawa, T. Oura, S. Oue, S.L. Walston, H. Takita, S. Matsushita, Y. Mitsuyama, T. Shimono, Y. Miki, and D. Ueda. 2024. Comparing the Diagnostic Performance of GPT-4-based ChatGPT, GPT-4V-based ChatGPT, and Radiologists in Challenging Neuroradiology Cases. *Clinical neuroradiology*.

Hou, R.Z., C. Chen, R. Sukthankar, and M. Shah. 2019. An Efficient 3D CNN for Action/Object Segmentation in Video. *British Machine Vision Conference*.

Landgren, O., P. Sonneveld, A. Jakubowiak, M. Mohty, K.S. Iskander, K. Mezzi, and D.S. Siegel. 2019. Carfilzomib with immunomodulatory drugs for the treatment of newly diagnosed multiple myeloma. *Leukemia*.

Laubach, J. 2019. Initial Therapy in Older Patients with Multiple Myeloma. *The New England journal of medicine*. 380:2172-2173.

Liu, C., J. Yuen, A. Torralba, and W.T. Freeman. 2011. SIFT Flow: Dense Correspondence across Scenes and Its Applications *IEEE Transactions on Pattern Analysis and Machine Intelligence* 33:978 - 994.

Logie, E., B. Van Puyvelde, B. Cuypers, A. Schepers, H. Berghmans, J. Verdonck, K. Laukens, L. Godderis, M. Dhaenens, D. Deforce, and W. Vanden Berghe. 2021. Ferroptosis Induction in Multiple Myeloma Cells Triggers DNA Methylation and Histone Modification Changes Associated with Cellular Senescence. *International journal of molecular sciences*. 22.

Lonial, S. 2010. Relapsed multiple myeloma. *Hematology Am Soc Hematol Educ Program*. 2010:303-309.

Lotvall, J., A.F. Hill, F. Hochberg, E.I. Buzas, D. Di Vizio, C. Gardiner, Y.S. Gho, I.V. Kurochkin, S. Mathivanan, P. Quesenberry, S. Sahoo, H. Tahara, M.H. Wauben, K.W. Witwer, and C. Thery. 2014. Minimal experimental requirements for definition of extracellular vesicles and their functions: a position statement from the International Society for Extracellular Vesicles. *J Extracell Vesicles*. 3:26913.

Matov, A. 2024a. Mitosis, Cytoskeleton Regulation, and Drug Resistance in Receptor Triple Negative Breast Cancer. *medRxiv*:2024/311425.

Matov, A. 2024b. Quantitative Video Microscopy in Medicine. *SSRN*:2024/4909309.

Matov, A. 2024c. A Real-Time Suite of Biological Cell Image Analysis Software for Computers, Smartphones, and Smart Glasses, Suitable for Resource-Constrained Computing. *arXiv*:2407.15735.

Matov, A. 2024d. Urinary Biomarkers for Disease Detection. *medRxiv*:2024.07.30.24311186.

Matov, A., K. Applegate, P. Kumar, C. Thoma, W. Krek, G. Danuser, and T. Wittmann. 2010. Analysis of microtubule dynamic instability using a plus-end growth marker. *Nature Methods*. 7:761- 768.

Matov, A., A. Bacconi, and J.C. Gatlin. 2024. Instantaneous Flow Analysis of Contractile Cytoskeletal Structures Affected by the Dysregulation of Kinesin and Tropomyosin Motors. *bioRxiv*:2024.06.28.601275.

Matov, A., and S. Modiri. 2024. Quantitative Microscopy in Medicine. *medRxiv*:2024/311304.

Matulis, S.M., V.A. Gupta, A.K. Nooka, H.V. Hollen, J.L. Kaufman, S. Lonial, and L.H. Boise. 2016. Dexamethasone treatment promotes Bcl-2 dependence in multiple myeloma resulting in sensitivity to venetoclax. *Leukemia*. 30:1086-1093.

McIntyre, O.R. 1979. Multiple Myeloma. 301:193-196.

Mollinedo, F., J. de la Iglesia-Vicente, C. Gajate, A. Estella-Hermoso de Mendoza, J.A. Villa-Pulgarin, M.A. Campanero, and M.J. Blanco-Prieto. 2010. Lipid raft-targeted therapy in multiple myeloma. *Oncogene*. 29:3748-3757.

Orkin, S.H., and L.I. Zon. 2008. SnapShot: hematopoiesis. *Cell*. 132:712.

Palumbo, A., and K. Anderson. 2011. Multiple myeloma. *The New England journal of medicine*. 364:1046-1060.

Pichiorri, F., S.S. Suh, M. Ladetto, M. Kuehl, T. Palumbo, D. Drandi, C. Taccioli, N. Zanesi, H. Alder, J.P. Hagan, R. Munker, S. Volinia, M. Boccadoro, R. Garzon, A. Palumbo, R.I. Aqeilan, and C.M. Croce. 2008. MicroRNAs regulate critical genes associated with multiple myeloma pathogenesis. *Proc Natl Acad Sci U S A*. 105:12885-12890.

Plebanek, M.P., R.K. Mutharasan, O. Volpert, A. Matov, J.C. Gatlin, and C.S. Thaxton. 2015. Nanoparticle Targeting and Cholesterol Flux Through Scavenger Receptor Type B-1 Inhibits Cellular Exosome Uptake. *Sci Rep*. 5:15724.

Prince, H.M., M. Bishton, and S. Harrison. 2008. The potential of histone deacetylase inhibitors for the treatment of multiple myeloma. *Leuk Lymphoma*. 49:385-387.

Raje, N., and D.L. Longo. 2015. Monoclonal Antibodies in Multiple Myeloma Come of Age. *The New England journal of medicine*. 373:1264-1266.

Ren, Z., Y. Su, and X. Liu. 2024. ChatGPT-Powered Hierarchical Comparisons for Image Classification. *NIPS '23: Proceedings of the 37th International Conference on Neural Information Processing Systems*:69706 - 69718.

Roccaro, A.M., A. Sacco, B. Thompson, X. Leleu, A.K. Azab, F. Azab, J. Runnels, X. Jia, H.T. Ngo, M.R. Melhem, C.P. Lin, D. Ribatti, B.J. Rollins, T.E. Witzig, K.C. Anderson, and I.M. Ghobrial. 2009. MicroRNAs 15a and 16 regulate tumor proliferation in multiple myeloma. *Blood*. 113:6669-6680.

Rublee, E., V. Rabaud, K. Konolige, and G. Bradski. 2011. ORB: an efficient alternative to SIFT or SURF. *International Conference on Computer Vision*:2564-2571.

Scovanner, P., S. Ali, and M. Shah. 2007. A 3-dimensional sift descriptor and its application to action recognition. *In* Proceedings of the 15th ACM international conference on Multimedia. ACM, Augsburg, Germany. 357-360.

Shi, J., and C. Tomasi. 1994. Good features to track. *IEEE Conference on Computer Vision and Pattern Recognition*:593 - 600.

Silva, A., M.C. Silva, P. Sudalagunta, A. Distler, T. Jacobson, A. Collins, T. Nguyen, J. Song, D.T. Chen, L. Chen, C. Cubitt, R. Baz, L. Perez, D. Rebatchouk, W. Dalton, J. Greene, R. Gatenby, R. Gillies, E. Sontag, M.B. Meads, and K.H. Shain. 2017. An Ex Vivo Platform for the Prediction of Clinical Response in Multiple Myeloma. *Cancer Res*. 77:3336-3351.

Spicka, I., E.M. Ocio, H.E. Oakervee, R. Greil, R.H. Banh, S.Y. Huang, J.M. D'Rozario, M.A. Dimopoulos, S. Martinez, S. Extremera, C. Kahatt, V. Alfaro, A.M. Carella, N. Meuleman, R. Hajek, A. Symeonidis, C.K. Min, P. Cannell, H. Ludwig, P. Sonneveld, and M.V. Mateos. 2019. Randomized phase III study (ADMYRE) of plitidepsin in combination with dexamethasone vs. dexamethasone alone in patients with relapsed/refractory multiple myeloma. *Ann Hematol*. 98:2139-2150.

Thery, C., K.W. Witwer, E. Aikawa, M.J. Alcaraz, J.D. Anderson, R. Andriantsitohaina, A. Antoniou, T. Arab, F. Archer, G.K. Atkin-Smith, D.C. Ayre, J.M. Bach, D. Bachurski, H. Baharvand, L. Balaj, S. Baldacchino, N.N. Bauer, A.A. Baxter, M. Bebawy, C. Beckham, A. Bedina Zavec, A. Benmoussa, A.C. Berardi, P. Bergese, E. Bielska, C. Blenkiron, S. Bobis-Wozowicz, E. Boilard, W. Boireau, A. Bongiovanni, F.E. Borras, S. Bosch, C.M. Boulanger, X. Breakefield, A.M. Breglio, M.A. Brennan, D.R. Brigstock, A. Brisson, M.L. Broekman, J.F. Bromberg, P. Bryl-Gorecka, S. Buch, A.H. Buck, D. Burger, S. Busatto, D. Buschmann, B. Bussolati, E.I. Buzas, J.B. Byrd, G. Camussi, D.R. Carter, S. Caruso, L.W. Chamley, Y.T. Chang, C. Chen, S. Chen, L. Cheng, A.R. Chin, A. Clayton, S.P. Clerici, A. Cocks, E. Cocucci, R.J. Coffey, A. Cordeiro-da-Silva, Y. Couch, F.A. Coumans, B. Coyle, R. Crescitelli, M.F. Criado, C. D'Souza-Schorey, S. Das, A. Datta Chaudhuri, P. de Candia, E.F. De Santana, O. De Wever, H.A. Del Portillo, T. Demaret, S. Deville, A. Devitt, B. Dhondt, D. Di Vizio, L.C. Dieterich, V. Dolo, A.P. Dominguez Rubio, M. Dominici, M.R. Dourado, T.A. Driedonks, F.V. Duarte, H.M. Duncan, R.M. Eichenberger, K. Ekstrom, S. El Andaloussi, C. Elie-Caille, U. Erdbrugger, J.M. Falcon-Perez, F. Fatima, J.E. Fish, M. Flores-Bellver, A. Forsonits, A. Frelet-Barrand, et al. 2018. Minimal information for studies of extracellular vesicles 2018 (MISEV2018): a position statement of the International Society for Extracellular Vesicles and update of the MISEV2014 guidelines. *J Extracell Vesicles*. 7:1535750.

Wang, J., A. Hendrix, S. Hernot, M. Lemaire, E. De Bruyne, E. Van Valckenborgh, T. Lahoutte, O. De Wever, K. Vanderkerken, and E. Menu. 2014. Bone marrow stromal cell-derived exosomes as communicators in drug resistance in multiple myeloma cells. *Blood*. 124:555-566.

Zhang, W., Y. Gu, Q. Sun, D.S. Siegel, P. Tolias, Z. Yang, W.Y. Lee, and J. Zilberberg. 2015. Ex Vivo Maintenance of Primary Human Multiple Myeloma Cells through the Optimization of the Osteoblastic Niche. *PLoS One*. 10:e0125995.

Zhang, W., W.Y. Lee, D.S. Siegel, P. Tolias, and J. Zilberberg. 2014. Patient-specific 3D microfluidic tissue model for multiple myeloma. *Tissue Eng Part C Methods*. 20:663-670.

Zheng, Y., C. Tu, J. Zhang, and J. Wang. 2019. Inhibition of multiple myelomaderived exosomes uptake suppresses the functional response in bone marrow stromal cell. *Int J Oncol*. 54:1061-1070.